Partial Near-Field Antenna Characterization

Amedeo Capozzoli, *Member, IEEE*, Claudio Curcio, *Member, IEEE*, and Angelo Liseno

***Abstract*— In some applications, the whole characterization (WC) of the antenna far-field pattern (FFP) by means of a near-field (NF) data, is not strictly required, but, on the contrary, just the partial knowledge of the FFP, along some cuts, is of interest. A new approach for the partial reconstruction is here presented: assigned the specifications on the partial characterization (PC) in terms of FFP cuts to be evaluated and tolerable characterization error, the proposed general strategy determines, in a rigorous mathematical framework, the optimal distribution of the measurement points in the NF, reduced in number with the respect to the WC, which shortens the acquisition time. The approach has been validated through a wide numerical and experimental analysis.**

***Index Terms*— Antenna measurements, fast characterization, near-field (NF), partial characterization (PC).**

NOMENCLATURE

$\mathcal{D}_{\text{ap}}$	Radiating aperture resembling the AUT (see Fig. 1).
a_{ap}, b_{ap}	Length of the aperture $\mathcal{D}_{\text{ap}}$ along x, y (see Fig. 1).
$\mathcal{D}$	Rectangular Measurement domain (see Fig. 1).
a, b	Length of the measurement domain $\mathcal{D}$ along x,y (see Fig. 1).
d	Measurement distance: location of $\mathcal{D}$ along z (see Fig. 1).
E_a	Aperture field (scalar modeling).
E_d	Field measured over $\mathcal{D}$ (scalar modeling).
F	Far field pattern (scalar modeling).
$\Phi_i[w, c_w]$	ith 1D PSWFs with "space-bandwidth product" cw.
β	Wavenumber.
a_{nm}	Coefficients expanding the aperture field E_a.
$\underline{a}$	Vector containing the a_{nm}.
u, v	Cosine directors related to the observation direction.
ξ, χ	Values between 0 and 1 defining the size of the observation region along u and v, respectively.
λ	Wavelength.
N, M	Number of PSWFs along x, y.
P	P = N∗M.
Q	Number of sampling points.
$\underline{r}_i$	Vector containing the coordinates of the ith sampling point.
$\mathcal{T}$	Near field radiation operator.
$\underline{b}$	Vector containing the measured voltages.
$\mathcal{A}$	subspace of the expansion coefficients vectors.
$\mathcal{B}$	$\mathcal{B} = \mathcal{T}(\mathcal{A})$ subspace of the measured voltages vectors.
$\mathcal{R}$	Far field radiation operator.
L	Number of the observation directions.
(u_i, v_i)	ith observation direction.
$\underline{\underline{T}}$	Matrix representing $\mathcal{T}$.
$\underline{\underline{R}}$	Matrix representing $\mathcal{R}$.
$\underline{\underline{U}}_R$, $\underline{\underline{\Sigma}}_R$, $\underline{\underline{V}}_R$	Matrices used in the SVD of $\underline{\underline{R}}$ [see (4)].
P_1	Number of the relevant singular values of $\underline{\underline{R}}$, size of the subspace $\mathcal{A}_1$.
$P_2 = (P\text{-}P_1)$	Size of the subspace $\mathcal{A}_2$.
$\mathcal{A}_1$, $\mathcal{A}_2$	Subspaces of $\mathcal{A}$: $\mathcal{A}$ is the direct sum of $\mathcal{A}_1$ and $\mathcal{A}_2$.
$\underline{a}_1$, $\underline{a}_2$	Vectors related to $\underline{a}$ [see (6)].
$\underline{a}'_1$, $\underline{a}'_2$	Components of $\underline{a}_1$ and $\underline{a}_2$, [see (7)].
$\mathcal{B}_1$, $\mathcal{B}_2$	Subspaces images of $\mathcal{A}_1$ and $\mathcal{A}_2$, respectively, through $\mathcal{T}$.
$\underline{b}_1$, $\underline{b}_2$	Vectors related to $\underline{b}$ [see (8)], images of $\underline{a}_1$ and $\underline{a}_2$, respectively, through $\underline{\underline{T}}$.
$\underline{\underline{T}}_1$, $\underline{\underline{T}}_2$	Matrices obtained from $\underline{\underline{T}}$ [see (9)].
D1	Distribution of the NF points obtained by applying the SVO to the problem in (10).
ϱ	Ratio between the l^2 norms of $\underline{b}_1$ and $\underline{\underline{P}}_1 \cdot \underline{b}_2$.
$\underline{\underline{U}}_1$ and $\underline{\underline{U}}_2$	Matrices containing the relevant LSVs of $\underline{\underline{T}}_1$ and $\underline{\underline{T}}_2$, respectively.
$\underline{\underline{P}}_1$	Matrix representing the orthogonal projector onto $\mathcal{B}_1$.
$\underline{\underline{U}}$	Matrix defined after (11).
D2	Distribution of NF points added to D1.
Θ	Minimum principal angle between B_1 and B_2.
$\underline{\underline{R}}_1^{\dagger}$	The pseudoinverse of $\underline{\underline{R}}_1 = \underline{\underline{R}} \cdot \underline{\underline{V}}_{R1}$.
$\underline{\underline{S}}_1$	$\underline{\underline{S}}_1 = \underline{\underline{T}}_1 \cdot \underline{\underline{R}}_1^{\dagger}$ is the matrix linking the FFP to the data.
ε_{max}	Bound for the relative error on the FFP.
$\bar{\varepsilon}_{max}$	Bound for the relative error on the normalized FFP.
κ_{S1}	The condition number of the matrix $\underline{\underline{S}}_1$.
ϵ_{amp}	Relative error on the pattern amplitude.
$\bar{\epsilon}_{amp}$	Relative error on the normalized pattern amplitude.
ϵ_{Dmax}	Relative error on the maximum directivity.
ϵ_{3db}	Relative error on the 3 dB beamwidth.

Manuscript received 17 July 2023; revised 31 May 2024; accepted 17 June 2024. Date of publication 3 July 2024; date of current version 8 October 2024. *(Corresponding author: Amedeo Capozzoli.)*

The authors are with the Dipartimento di Ingegneria Elettrica e delle Tecnologie dell'Informazione, Università di Napoli Federico II, 80125 Naples, Italy (e-mail: a.capozzoli@unina.it; clcurcio@unina.it; angelo.liseno@unina.it).

Color versions of one or more figures in this article are available at https://doi.org/10.1109/TAP.2024.3420093.

Digital Object Identifier 10.1109/TAP.2024.3420093

ϵ_{SLL}	Relative error on the first sidelobe.
T_x and T_y	Factors defining the amplitude tapering of the aperture field along x and y, respectively.
S_x and S_y	Factor defining the quadratic defocusing of the aperture field phase along x and y, respectively.
T_{xy}	Factors defining a circular amplitude tapering of the aperture field.
ϵ_{bp}	Relative error on the beampointing direction.

I. Introduction

THE reduction of the measurement time is a key-point in the framework of near-field (NF) antenna measurements. Indeed, depending on the particular antenna under test (AUT), the characterization time can become quite long. Among the others, this is the case of antennas with several ports, working on different frequency bands or in different working configurations (for instance, beam switching), as base station antennas or phased arrays, whose whole characterization (WC) can be very time-consuming [1]. Obviously, long-lasting characterizations lead to high costs in the design and manufacturing process.

Fast NF characterization techniques have been developed through the years, aimed at reducing the number of collected NF samples and/or the scanning path length [2], [3], [4]. Anyway, for the mentioned cases, the measurements can remain long-lasting or useless if the whole far-field pattern (FFP) is not of interest.

Indeed, all the standard as well as optimized characterization approaches are, generally speaking, aimed to reconstruct the whole FFP, and so they will be referred, in the following, as WC techniques. Nevertheless, in several cases, the knowledge of the whole FFP is not strictly required, but the real interest is in the behavior along the cuts, thus realizing a partial characterization (PC). The proposed PC method is of interest as long as a NF test range is available instead of an adequate far-field test range or a compact test range. On the other hand, PC can be of interest in in-series characterizations of antennas on a manufacturing line: in this case, a simplified NF setup could be used which profits of the reduced number of the optimized distribution of the samples. Accordingly, driven by fast characterization requirements, the following questions arise.

1) Are all the NF data used in the WC really needed for a PC, that is, to reconstruct the FFP just along some cuts?
2) Alternatively, depending on the particular AUT, is it possible to define a strategy determining the minimum number of samples and their spatial distribution to get a goal less ambitious than the whole antenna characterization?

Some interesting PC methods have been proposed in the recent years [5], [6]. Both the approaches refer to a spherical NF scanning. The approach in [5] is suited for linear antennas or apertures and arrays with separable excitations, and is based on the measurement of the NF along two cuts to retrieve the FFP along the principal cuts. In [6], single FFP cuts are obtained from spherical NF rings, and, unlike [5], probe compensation is allowed: the approach provides reconstruction errors, depending on the cuts of interest and the measuring distance. Both the methods allow better results when separable sources are considered. The approach in [5] has been also extended to the phaseless case [7].

The aim of this article is to present a general strategy to determine the distribution of the measurement points needed to perform the required PC, shortening the measurement process with respect to WC. The strategy exploits a priori information about the antenna to select only those measurement locations which are strictly required to get a prediction of the FFP along the cut of interest.

To define the sampling points distribution, the proposed PC approach [8], [9] exploits the singular value optimization (SVO) concept [2], [3], which is based on the following points.

1) The NF characterization is formulated as a linear inverse problem aiming to retrieve the (visible) aperture field (AF), starting from the measured NF data.
2) The SVO determines the optimal number and distribution of the NF samples as the ones optimizing the behavior of the singular values (SVs) of the relevant operator.

The SVO has been fruitfully applied, in the case of WC, to different kinds of antennas and scanning geometries [2], [3]. It determines a drastic reduction of the measurement time with respect to standard as well as nonconventional approaches, by reducing the number of samples and the scanning path length.

Here we refer to aperture antennas and NF planar scanning systems. Nevertheless, the hypothesis of aperture modeling is not mandatory: the approach allows optimal results as long as an effective mathematical description of the radiation is available.

The idea of the proposed PC technique has been briefly presented in [8] and [9]. Here, a deep detailed discussion is reported. A wide numerical analysis shows the performance of the method that has been also experimentally validated.

The article is organized as follows. Section II is devoted to recall the relevant aspects of the previous works: the NF characterization is formulated as a linear inverse problem, and the SVO is briefly summarized. In Section III the NF characterization is reformulated under the PC point of view, and a strategy is presented for the determination of the optimal distribution of NF samples. The method has been validated numerically (Section IV) and experimentally (Section V). Conclusion is drawn in Section VI.

II. NF Characterization as a Linear Inverse Problem: the SVO Idea

Let us consider a rectangular aperture $\mathcal{D}_{ap}$, of size $2a_{ap} \times 2b_{ap}$, resembling the AUT centered in the Oxyz reference system (Fig. 1), and let us assume the radiated field measured on a rectangular measurement domain $\mathcal{D}$, 2a $\times$ 2b sized, located in the plane $z = d$.

To simplify the discussion, a scalar case is considered, with a linearly polarized AF, say $\underline{E}_a = E_a \hat{\imath}_y$, a measured field on

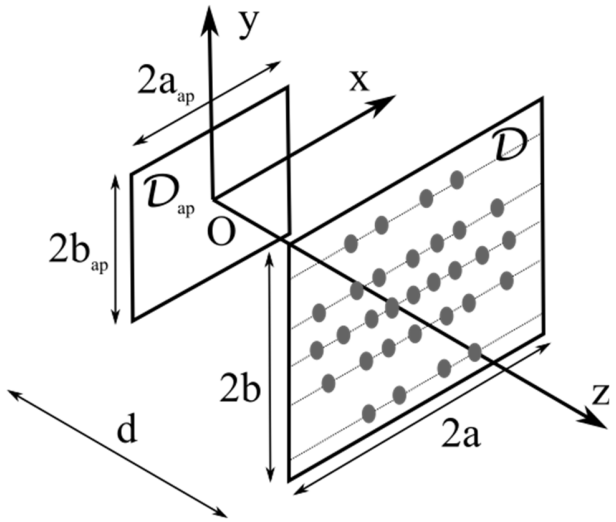

Fig. 1. Geometry of the problem.

$\mathcal{D}$ linearly polarized along y, say $E_d\hat{i}_y$, and a scalar FFP, say F, representing the relevant Cartesian component.

The evaluation of the FFP from NF data amounts to determine E_a from E_d, and then to calculate F using the FF operator. Given the two FFP Cartesian components, the spherical or the co-polar and cross-polar ones can be easily calculated.

By exploiting the a priori information about the dimension of $\mathcal{D}_{ap}$, E_a can be assumed as an element of a finite dimensional subspace, say $\mathcal{E}$. More in detail, E_a can be represented by the visible prolate spheroidal wave functions (PSWFs), which are the optimal choice [1], [2], [10]

$$E_a(x, y) = \sum_{n=1}^{N}\sum_{m=1}^{M} a_{nm}\Phi_n[x, c_x]\Phi_m[y, c_y] \tag{1}$$

where $\Phi_i[w, c_w]$ is the ith 1-D PSWFs with "space-bandwidth product" c_w,

1) $u = \sin\theta\cos\varphi$ and $v = \sin\theta\sin\varphi v = \sin\theta\sin\varphi$, θ and φ being the standard spherical coordinates in the Oxyz system (see Fig. 1).
2) $c_x = a_{ap}\beta\xi$ and $c_y = b_{ap}\beta\chi$, β being the wavenumber, ξ and χ being real numbers in the range [0, 1] which define the observation directions wherein F is required (typically $\xi = \chi = 1$).
3) $N = \text{Int}[4a_{ap}/\lambda]$ and $M = \text{Int}[4b_{ap}/\lambda]$, λ being the wavelength and Int[·] denoting the integer part of its argument.

The numerical evaluation of the PSWFs has been performed following the approach in [11], bringing the problem back to the inversion of a tridiagonal matrix. At variance with the classical Bowkamp's [12] approach exhibiting a computational complexity growing as $O(n^2)$, where n is the number of PSWFs to be computed, the approach here adopted uses a purposely tailored Gaussian Quadrature to guarantee numerical stability and shows a computational complexity growing as O(n + c log c), c being the space-bandwidth product [13].

Accordingly, E_a, E_d, and F are assumed as belonging to subspaces of dimension $P = NM$.

Let us denote with Q the number of sampling points on $\mathcal{D}$, and with $\underline{r}_1, \ldots, \underline{r}_Q$ their vector positions. The NF operator $\mathcal{T}$ is represented by the matrix $\underline{\underline{T}}$ linking the vector $\underline{a} \in \mathcal{A} = \mathbb{C}^P$, containing the P expansion coefficients in (1) to the vector $\underline{b} \in \mathcal{B} = \mathbb{C}^Q$, containing the field samples at $\underline{r}_1, \ldots, \underline{r}_Q$

$$\underline{\underline{T}} \cdot \underline{a} = \underline{b}. \tag{2}$$

The expression of $\underline{\underline{T}}$ can be evaluated following different approaches [2], [3]: one option is the plane-waves expansion. $\underline{\underline{T}}$ depends on Q and the locations $(\underline{r}_1, \ldots, \underline{r}_Q)$ as parameters. Accordingly, a family of matrices is at disposal, and the SVO selects, among all of them, the most convenient one in terms of conditioning. The SVO solves the sampling problem by determining Q and the $(\underline{r}_1, \ldots, \underline{r}_Q)$ by optimizing, through an iterative procedure, a functional measuring the SV behavior of $\underline{\underline{T}}$, say Ξ [2], [3], [14]. More in detail, at the beginning Q is set equal to P, and the $(\underline{r}_1, \ldots, \underline{r}_Q)$ are found by maximizing Ξ. Then, Q is updated to $Q + 1$, and new optimization of Ξ updates the positions $(\underline{r}_1, \ldots, \underline{r}_{Q+1})$. The iterative process is stopped when the curve describing the maximum value of Ξ as function of Q saturates. The $(\underline{r}_1, \ldots, \underline{r}_Q)$ corresponding to the saturation are assumed as the sampling points.

Once the optimal values of Q and $(\underline{r}_1, \ldots, \underline{r}_Q)$ are identified, $\underline{\underline{T}}$ is known and E_a can be calculated after a regularized inversion of (2) [2], [3]. As final remark it is noted that optimal Q is related to the dimension P of the linear subspace to which the unknown $\underline{a}$ belongs.

III. PC Approach

The basic idea of the proposed PC approach is based on two key properties.

1) Only a subspace of $\mathcal{E}$ contributes to calculation of F along the desired cut.
2) Typically, the dimension of this subspace is less then $\dim(\mathcal{E}) = P$.

As a consequence, the number of the NF samples required for the PC is expected to be smaller than that needed for the WC, as long as it is possible to identify and measure only the relevant NF, that is, that part of the NF which contributes to F along the cut of interest.

Here, the strategy required to define the distribution of the sampling points needed to catch the relevant NF as is presented. As highlighted in the following, a priori information about the source is needed to take advantage, at the best, of the PC approach. In many cases, the antenna engineer has an idea, possibly rough, of the FFP features. In some cases, more detailed information is available as happens for in-series characterizations of antennas on a manufacturing line, as well as when simulations on the AUT are available.

Let us now introduce formally the FF operator represented by the matrix $\underline{\underline{R}}$ linking $\underline{a}$ to the vector $\underline{f} \in \mathbb{C}^L$, containing the values of F over the L observation directions of interest $(u_1, v_1), \ldots, (u_L, v_L)$

$$\underline{\underline{R}} \cdot \underline{a} = \underline{f}. \tag{3}$$

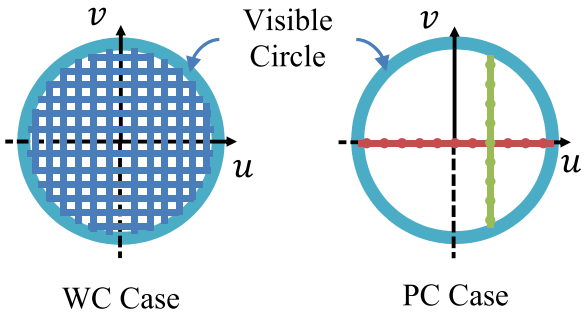

Fig. 2. WC and PC observation sets for the PC case just two examples are reported, the u-cut for $v = 0$ (red dots) and a generic v-cut (green dots).

The FF operator is strictly related to a 2-D spatial Fourier Transform [15].

In the case of a WC, typically, the set of the observation directions spans the whole visible domain (see Fig. 2) with a large value of L. On the contrary, in the PC case, the observation set is made up of a subset of directions in the visible domain and the corresponding value of L can be much smaller than that of the WC case. Sketches of the observation sets, for the WC and the PC cases, are reported in Fig. 2. For the PC case, two classical choices are depicted: a u-cut (red dots) and a v-cut (green dots).

The PC approach is illustrated highlighting three key points.

1) Segmentation of $\mathcal{A}$ into two orthogonal subspaces, say $\mathcal{A}_1$, and $\mathcal{A}_2$, and resulting segmentation of $\mathcal{B}$ into two subspaces, say $\mathcal{B}_1$, and $\mathcal{B}_2$ as in Section III-A.
2) Segmentation of $\underline{b}$ into two contributions, $\underline{b}_1 \in \mathcal{B}_1$ and $\underline{b}_2 \in \mathcal{B}_{2\text{in}}$ as in Section III-B.
3) Extraction from $\underline{b}$ of the Relevant NF as in Section III-C.

A workflow summarizes the procedure in Section III-D.

In the following, for the sake of brevity, the PC will consider only cuts of the visible domain such as a u-cut, that is, a cut with v fixed, or a v-cut, that is, a cut with u fixed. Other options are possible thanks to the generality of the approach.

A. Segmentation of $\mathcal{A}$

By applying the SV decomposition, $\underline{\underline{R}}$ can be written as [16]

$$\underline{\underline{R}} = \underline{\underline{U}}_R \cdot \underline{\underline{\Sigma}}_R \cdot \underline{\underline{V}}_R^H \tag{4}$$

where $\underline{\underline{U}}_R$ is the $L \times L$ matrix containing the left singular vectors (LSV) of $\underline{\underline{R}}$, $\underline{\underline{V}}_R$ is the $P \times P$ matrix containing the right singular vectors (RSV) of $\underline{\underline{R}}$, $\underline{\underline{\Sigma}}_R$ is the $L \times P$ diagonal matrix containing the SVs of $\underline{\underline{R}}$. The apex H stands for Hermitian conjugate.

Let us denote with P_1 the number of significant SVs of $\underline{\underline{R}}$, that is, the number of SVs larger than a prefixed threshold, specified according to the expected accuracy on the reconstruction.

When WC is of interest, the large values for L make P_1 close to $P = NM$, that is, to the number of basis function expanding the visible AF. On the contrary, in the PC case, the small values for L make P_1 smaller than P. Once P_1 has been evaluated, $\mathcal{A}$ can be decomposed as the direct sum of two orthogonal subspaces $\mathcal{A}_1$, having dimension P_1, and $\mathcal{A}_2$, having dimension $P_2 = (P - P_1)$. More in detail, after writing $\underline{\underline{V}}_R$ as

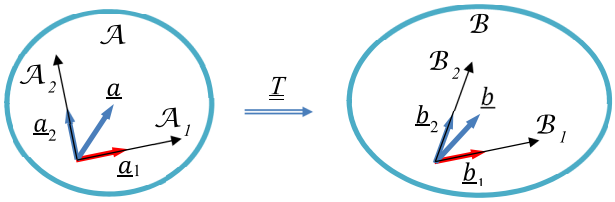

Fig. 3. Decomposition $\underline{a}$ and $\underline{b}$; $\underline{a}_1$ and $\underline{b}_1$ are highlighted in red.

$$\underline{\underline{V}}_R = \begin{bmatrix} \underline{\underline{V}}_{R1} & \underline{\underline{V}}_{R2} \end{bmatrix} \tag{5}$$

where $\underline{\underline{V}}_{R1}$ and $\underline{\underline{V}}_{R2}$ are submatrices with size $P \times P_1$ and $P \times P_2$, respectively, we can define $\mathcal{A}_1 = span\{\underline{\underline{V}}_{R1}\}$, the subspace of $\mathcal{A}$ providing relevant contributions to F, and $\mathcal{A}_2 = span\{\underline{\underline{V}}_{R2}\}$, the subspace of $\mathcal{A}$ orthogonal to $\mathcal{A}_1$ which does not provide appreciable contributions to F.

Accordingly, each vector $\underline{a}$ can be written as

$$\underline{a} = \underline{a}_1 + \underline{a}_2 \tag{6}$$

where $\underline{a}_1 \in \mathcal{A}_1$ and $\underline{a}_2 \in \mathcal{A}_2$ are uniquely identified. In Fig. 3, the decomposition of $\mathcal{A}$ into two orthogonal subspaces is schematically depicted by highlighting the decomposition of a vector $\underline{a}$, and the vector $\underline{a}_1$ in red.

It is noted that $\underline{a}_1$ and $\underline{a}_2$ are P-sized vectors, belonging, respectively, to a P_1-sized and a P_2-sized subspace. Therefore, it is convenient to introduce their P_1-sized and a P_2-sized representations, $\underline{a}'_1$ and $\underline{a}'_2$, respectively

$$\begin{cases} \underline{a}'_1 = \underline{\underline{V}}_{R1}^H \underline{a} \\ \underline{a}'_2 = \underline{\underline{V}}_{R2}^H \underline{a}. \end{cases} \tag{7}$$

Given $\mathcal{A}_1$ and $\mathcal{A}_2$, the decomposition of $\mathcal{B}$, which generally is not orthogonal, follows immediately: $\mathcal{B}_1 = \mathcal{T}(\mathcal{A}_1)$ and $\mathcal{B}_2 = \mathcal{T}(\mathcal{A}_2)$.

B. Segmentation of $\underline{b}$

Following (6), $\underline{b}$ can be written as the sum of two contributions

$$\underline{b} = \underline{b}_1 + \underline{b}_2 = \underline{\underline{T}} \cdot \underline{a}_1 + \underline{\underline{T}} \cdot \underline{a}_2 \tag{8}$$

where $\underline{b}_1$ is the Q-sized vector representing that part of $\underline{b}$ useful to retrieve F, and $\underline{b}_2$ is the Q-sized vector representing that part of $\underline{b}$ not contributing to F. Unlike $\underline{a}_1$ and $\underline{a}_2$, generally $\underline{b}_1$ and $\underline{b}_2$ are not orthogonal as schematically depicted in Fig. 3, since generally the mapping $\underline{\underline{T}}$ does not preserve the scalar product [17].

By using (7) and (8), $\underline{b}_1$ and $\underline{b}_2$ can be explicitly related to $\underline{a}'_1$ and $\underline{a}'_2$

$$\underline{b} = \underline{b}_1 + \underline{b}_2 = \underline{\underline{T}}_1 \cdot \underline{a}'_1 + \underline{\underline{T}}_2 \cdot \underline{a}'_2 \tag{9}$$

where

$$\begin{cases} \underline{\underline{T}}_1 = \underline{\underline{T}} \cdot \underline{\underline{V}}_{R1} \\ \underline{\underline{T}}_2 = \underline{\underline{T}} \cdot \underline{\underline{V}}_{R2} \end{cases} \tag{10}$$

and $\underline{\underline{T}}_1 \in \mathbb{C}^{Q\times P_1}$, $\underline{\underline{T}}_2 \in \mathbb{C}^{Q\times P_2}$.

If one were able to isolate $\underline{b}_1$, the NF contribution of interest, that is, if one were able to extract $\underline{b}_1$ from $\underline{b}$, $\underline{a}_1$ could be easily retrieved by solving the inverse problem for $\underline{\underline{T}}_1$

$$\underline{\underline{T}}_1 \cdot \underline{a}'_1 = \underline{b}_1. \tag{11}$$

Some remarks are in order.

The problem in (11) involves, at most, P_1 SVs, so that in principle, the number of measurements to reconstruct $\underline{a}_1$ can be quite smaller than that required by WC. A strategy to determine the number and the distribution of the NF samples needed to reconstruct $\underline{a}_1$ is required: the SVO is exploited here. Finally, the SVO applied to (11) determines the NF distribution of samples made of just one row or one column of nonuniformly spaced points, or few rows or few columns of nonuniformly spaced points, according to the requirements, say D1. In the article, D1 will consider just one row or one column of field samples, being the extension to more rows or columns straightforward.

It is worth noting that it is difficult to understand, a priori, if one row or one column, few rows or few columns are sufficient for the PC. The approach answers to this question, supported by a mathematical framework formally exploiting a priori information about the AUT. If the answer is positive, PC is possible from D1. If the answer is negative an additional distribution of samples is added, say D2, allowing PC.

The above discussion shows that the reconstruction of F is affordable if $\underline{b}_1$ can be calculated from $\underline{b}$.

C. Extraction of $\underline{b}_1$ From $\underline{b}$

After the measurement process, $\underline{b}$ is available. The calculation of $\underline{b}_1$ from $\underline{b}$ depends, clearly, on the relationship between $\underline{b}_2$ and $\underline{b}_1$, which is dictated not only by the AUT features but also by the peculiar NF samples distribution. Given the row or the column of D1, the field samples distribution on D1 is determined by applying SVO to $\underline{\underline{T}}_1$. Two procedures are exploited to extract $\underline{b}_1$ from $\underline{b}$ depending on the values of the parameter $\varrho = \|\underline{\underline{P}}_1 \cdot \underline{b}_2\|/\|\underline{b}_1\|$, where $\|\cdot\|$ denotes the l^2 norm, and $\underline{\underline{P}}_1$ is the matrix representing the orthogonal projector onto $\mathcal{B}_1$

$$\underline{\underline{P}}_1 = \underline{\underline{U}}_1 \cdot \underline{\underline{U}}_1^H \tag{12}$$

where $\underline{\underline{U}}_1$ is the matrix containing the relevant LSVs of $\underline{\underline{T}}_1$.

Case I: The first case correspond to "small" values of ϱ.

In this case $\underline{b}_2$ is neglected, and $\underline{f}$ is calculated after a regularized inversion (here a Truncated SVD) of

$$\underline{\underline{S}}_1 \cdot \underline{f} = \underline{b}_1 \tag{13}$$

being $\underline{\underline{R}}_1 = \underline{\underline{R}} \cdot \underline{\underline{V}}_{R1}$, $\underline{\underline{S}}_1 = \underline{\underline{T}}_1 \cdot \underline{\underline{R}}_1^{\dagger}$, and $\underline{\underline{R}}_1^{\dagger}$ the pseudoinverse of $\underline{\underline{R}}_1$.

Now, to find an estimate of the acceptable range of values for ϱ, a bound to the error on $\underline{f}$ due to neglecting $\underline{b}_2$ is provided. Actually, $\underline{b}_2$ in (13) can be seen as an additive "noise" to $\underline{b}_1$, quantified by ϱ. Consequently, an additive error $\underline{\delta f}$ affects $\underline{f}$. Equation (13) turns into

$$\underline{\underline{S}}_1 \cdot \left(\underline{f} + \underline{\delta f}\right) = \underline{b}_1 + \underline{\underline{P}}_1 \cdot \underline{b}_2. \tag{14}$$

By defining ε_{max} as the relative error bound on $\underline{f}$, we have

$$\frac{\left\|\underline{\delta f}\right\|}{\left\|\underline{f}\right\|} \le cond\left(\underline{\underline{S}}_1\right)\frac{\left\|\underline{\underline{P}}_1 \cdot \underline{b}_2\right\|}{\left\|\underline{b}_1\right\|} = cond\left(\underline{\underline{S}}_1\right)\varrho = \varepsilon_{max}. \tag{15}$$[1]

Given ϱ and $cond(\underline{\underline{S}}_1)$, ε_{max} is calculated. When the bound ε_{max} is coherent with the requirements, PC can be performed using the distribution D1. Obviously, an estimate, even rough of ϱ is a priori required. This information should be made available at the design/simulation stage of the AUT, or at the beginning of the in-series characterizations.

As a final remark it is noted that, if the experimental characterization of the AUT requires as output the normalized FFP, $\bar{\underline{f}} = (\underline{f}/\|\underline{f}\|_\infty)$,[2] the parameter $\bar{\varrho}$ instead of ϱ is in order

$$\bar{\varrho} = \frac{\left\|\underline{\underline{P}}_1 \cdot \underline{b}_2 - \frac{\underline{b}_1 \underline{b}_1^H \cdot \underline{b}_2}{\|\underline{b}_1\|^2}\right\|}{\left\|\underline{b}_1\right\|} \tag{16}$$

since the error along $\underline{b}_1$, $((\underline{b}_1 \underline{b}_1^H \cdot \underline{b}_2)/\|\underline{b}_1\|^2)$, is made irrelevant by normalization. In this case, the error bound $\bar{\varepsilon}_{max}$ becomes

$$\bar{\varepsilon}_{max} = cond\left(\underline{\underline{S}}_1\right)\bar{\varrho}. \tag{17}$$

In many cases $\bar{\underline{f}}$ is of practical interest instead of $\underline{f}$, for example, when features as beamwidth, sidelobe level, and beam-pointing angle are required, and, frequently, $\bar{\underline{f}}$ is depicted as FFP in the literature.

Case II: When ϱ is not "small" as in Case I, leading to an unacceptable ε_{max}, or when the estimate of ϱ is unreliable, D1 in insufficient and a different strategy should be adopted for PC. In this case $\underline{b}_2$ in not negligible and $\underline{b}_1$ has to be extracted from $\underline{b}$.

To this end a linear system of equations should be solved, which could be affected by an ill conditioning deteriorating the reliability of the solution. Accordingly, to improve reliability, the new set of NF points D2 should be added to D1. D2 is chosen as the one improving the minimum principal angle, say Θ, between $\mathcal{B}_1$ and $\mathcal{B}_2$ [16]. More in detail, starting from D1 further sampling points are iteratively added to increase Θ above a prescribed threshold. Using the data collected according to distribution D1 and D2, the two contributions $\underline{b}_1$ and $\underline{b}_2$ can be reliably estimated; then, $\underline{a}'_1$ can be retrieved and $\underline{f}$ evaluated.

For a value of Θ above the threshold, $\underline{b}_1$ and $\underline{b}_2$ are estimated after inverting the matrix $\underline{\underline{U}}$ defined as

$$\underline{\underline{U}} = \left[\underline{\underline{U}}_1 \quad \underline{\underline{U}}_2\right] \tag{18}$$

where $\underline{\underline{U}}_2$ is the matrix containing the relevant LSVs of $\underline{\underline{T}}_2$. It is noted that the conditioning number of $\underline{\underline{U}}$ decreases with Θ, showing that increasing Θ increases reliability of the estimate of $\underline{b}_1$.

As a final remark, it is stressed that the final distribution of samples given by D1 and D2 does not allow a WC reconstruction with an error comparable with that on PC. In other words, the distribution of the NF sampling points made of D1 and D2 has not been optimized to provide a

[1] $cond(\cdot)$ represents the conditioning number of the considered matrix.

[2] $\|\underline{x}\|_\infty := |x_i|$.

reliable estimation of a'_2, since the behavior of the SVs of $\underline{\underline{T}}_2$ has not been subjected to any optimization.

D. Workflow of the PC Approach

Given the maximum tolerable error (MTE), the approach provides an optimal distribution of the NF samples allowing the FFP evaluation with an error below MTE. The samples distribution is identified in two steps. In the first step, D1 is determined after applying the SVO to operator in (11) and ϱ and $cond(\underline{\underline{S}}_1)$ are evaluated. From ϱ and $cond(\underline{\underline{S}}_1)$, ε_{max} and $\bar{\varepsilon}_{max}$ are calculated exploiting (14) and (16), respectively. If the bound of interest is smaller than the given MTE and the value of ϱ is assumed reliable, PC is possible by using D1 only. On the contrary, an incremental distribution D2 should be added to D1, which increases the minimum principal angle between the two relevant subspaces, $\mathcal{B}_1$ and $\mathcal{B}_2$, until a reliable estimate of $\underline{b}_1$ can be obtained.

IV. Numerical Results

In this section the performances of the method are highlighted by presenting test cases involving both continuous aperture antennas and array antennas, with various features. In particular, AUT's are considered

1) With different sizes.
2) With separable and nonseparable AF.
3) Radiating shaped beams.
4) Radiating steered beams.

A scalar model is considered in all the cases involving arrays as well as in the first three cases involving apertures, while the fourth aperture case is a full-vector one.

Regarding the continuous apertures, four cases are examined. In the first cases, say AP1, the reconstructions along the principal cuts $u = 0$ and $v = 0$ are considered. Two excitations are considered, one separable and one nonseparable: in both cases D1 is sufficient to evaluate the FFP. The first excitation matches recommendations for PC given in the literature. The second one shows that PCs are possible also for nonseparable AFs, with benefits in terms of scanning path length and samples distribution with respect to WC. In the second case, say AP2, the distribution D1 gives an unacceptable error bound and D2 becomes mandatory. In the third case, say AP3, the reconstruction along the cut $u = v$ is considered. Finally, for the fourth case, say AP4, both the co-polar and cross-polar components are considered, by referring to the cut $v = 0$.

Regarding the arrays, two test cases are reported. As first test case, say Case AR1, an array radiating a shaped beam has been considered, while in the second case, say Case AR2, a steered beam is considered.

To evaluate the performance of the approach up to six error figures are considered, depending on the case of interest.

1) Relative error on pattern amplitude $\epsilon_{amp} = \| |\underline{f}|^2 - |\underline{f}_r|^2 \| / \| |\underline{f}|^2 \|$, where $\underline{f}_r$ is the retrieved pattern.
2) Relative error on the normalized pattern amplitude $\bar{\epsilon}_{amp} = \| |\bar{\underline{f}}|^2 - |\bar{\underline{f}}_r|^2 \| / \| |\bar{\underline{f}}|^2 \|$, where $\bar{\underline{f}}_r$ is the retrieved normalized pattern.
3) Relative error on the maximum directivity ϵ_{Dmax}.
4) Relative error on the 3 dB beamwidth ϵ_{3dB}.
5) Relative error on the first sidelobe ϵ_{SLL}.
6) Relative error on the beam-pointing angle ϵ_{bp}.

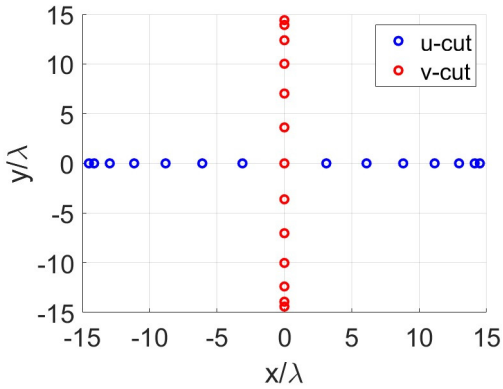

Fig. 4. Sampling point distribution D1 obtained for PC along the u-cut (blue markers) and the v-cut (red markers)—aperture $3\lambda \times 2.4\lambda$ sized, d = 10.8λ. The (0, 0) sample belongs to both the distributions.

Since the quality parameters are independent of the antenna efficiency they provide information about both directivity and gain. Results are presented by referring to directivity, evaluated after assuming that the known radiated power is as estimated from the WC characterization. Analogous results can be obtained for gain, but the additional WC is not required since the input power for the antenna is needed for this case.

PC is affected by two sources of error. The first is due to the reduced number of NF data. The second is due to the noise on the data. To evaluate the performance of the proposed PC method against noise on the data, some numerical test cases have been worked out by adding an independent and normally distributed random noise, with a signal-to-noise ratio of 40 dB. A total of 200 different noise realizations have been considered, and the error figures have been evaluated as mean values across the noise realizations.

A. Case AP1

All AP1 cases involve a continuous radiating aperture with $a_{ap} = 1.5\lambda$ and $b_{ap} = 1.2\lambda$, represented with $N = 6$ and $M = 5$ PSWFs, and $d = 10.8\lambda$ (see Fig. 1). The dimensions correspond to those of the standard gain horn Narda 640 working in the X-band which has been subject to the experimental analysis.

Two PCs, along the u-cut for $v = 0$, and along the v-cut for $u = 0$, have been considered. The approach gives D1's involving samples along the x-axis and the y-axis, respectively: 15 NF samples are required along the x-axis for the first PC, and 13 NF samples along the y-axis for the second PC. The D1 distributions of both cases are reported in Fig. 4, as blue and red circles, respectively. In both cases, the minimum distance between consecutive samples is about 0.45λ.

As first excitation, say Case AP1.1, a separable AF is assumed in the form

$$E_a(x, y) = e^{-\frac{T_x x'^2}{Np}} e^{-\frac{T_y y'^2}{Np}} e^{-j2\pi S_x x'^2} e^{-j2\pi S_y y'^2} \tag{19}$$

TABLE I
ERROR FIGURES (IN PERCENTAGE) OF THE NUMERICAL CASES

#	Case	Cut	Distrib.	ϵ_{amp}	$\bar{\epsilon}_{amp}$	ϵ_{Dmax}	ϵ_{3dB}	ϵ_{SLL}	ϵ_{bp}
1	AP1.1	v=0	D1	2.6	0.39	1.2	0	3.2	0
2		u=0	D1	2	0.40	0.9	0	0.5	0
3	AP1.2	v=0	D1	3.7	0.3	0.9	0	1.1	0
4	AP2	v=0	D1+D2	0.5	0.5	0.08	0	0.45	0
5			D1	13.5		7	0	5.7	0
6		u=0	D1+D2	0.2	0.26	0.09			
7			D1	25		19			
8	AP3	u=v	D1+D2	0.2	0.2	0.02	0		
9		u=v	D1	3.4		1.4	0		
10	AP4-COP	v=0	D1	1.5	0.03	0.5	0	0.02	0
11	AP4-CRO	v=0	D1	10	10				
12	AR1	v=0	D1+D2	0.2	0.2	0.01		0.22	
13			D1	10.5		3.5		1.22	
14	AR2	v=0.2	D1	7.8	0.3	1.9	0	0.24	0

where $x' = x/a_{ap}$, $y' = y/b_{ap}$, and Np = 8.686 dB, and T_x and T_y are in dB. Obviously, T_x and T_y control the amplitude tapering of AF (in dB), while S_x and S_y control the quadratic phase term of AF.

By setting $T_x = 20$ dB, $T_y = 0.5$ dB, $S_x = 0.19$ and $S_y = 0.11$, values of ϱ equal to about -30 and -20 dB are obtained for the u-cut and the v-cut case, respectively, leading to a satisfactory error bound. It is noted that the defocusing terms have been selected to account for the real geometry of the Narda 640 horn.

The directivity retrieved with the D1 (red line) is reported for the u-cut and the v-cut in Fig. 5(a) and (b), respectively, together with the numerical reference (blue crosses). As it can be seen a good agreement is obtained. The error figures for the u-cut and the v-cut are reported in the first and second rows of Table I, respectively.

The second excitation, say Case AP1.2, involves a nonseparable AF, in the form

$$E_a(x, y) = e^{-\frac{T_{xy}\sqrt{x^2+y^2}}{Np\sqrt{a_{ap}^2+b_{ap}^2}}} e^{-j2\pi S_x x'^2} e^{-j2\pi S_y y'^2} \qquad (20)$$

where T_{xy} is in dB.

For this case, for the sake of brevity, just the result for the PC along the u-cut is presented. By setting $T_{xy} = 6$ dB, $S_x = 0.19$, and $S_y = 0.11$, a value of ϱ equal to about -25 dB is obtained.

The corresponding directivity patterns are shown in in Fig. 5(c). Again, a good agreement is observed. The error figures are given in the third row of Table I.

B. Case AP2

This case refers to a continuous radiating aperture, larger than Case AP1, with $a_{ap} = 3.2\lambda$ and $b_{ap} = 1.8\lambda$, represented

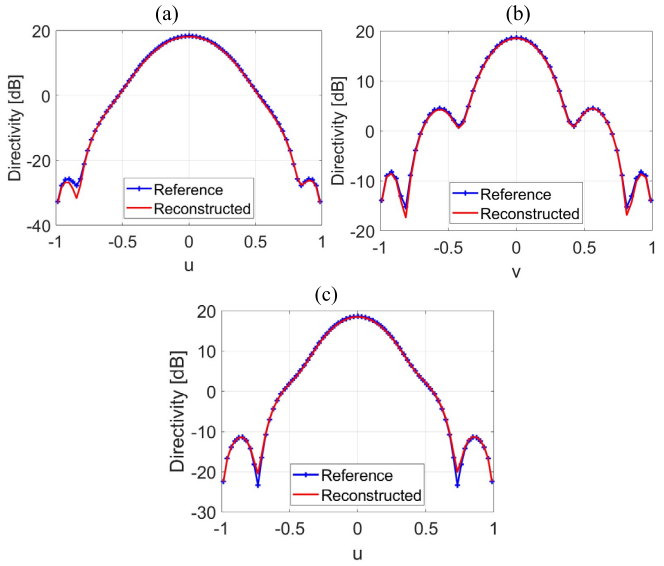

Fig. 5. Behavior of the reference directivity (blue crosses) and of the one reconstructed with the D1 (red line) for an aperture $3\lambda \times 2.4\lambda$ sized, $d = 10.8\lambda$. (a) Case AP1-E1, reconstruction along the u-cut for $v = 0$. (b) Case AP1.1, reconstruction along the v-cut for $u = 0$. (c) Case AP1.2, reconstruction along the u-cut for $v = 0$.

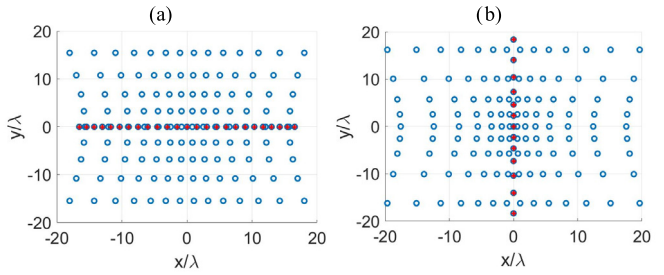

Fig. 6. Sampling point distribution for an aperture $6.4\lambda \times 3.6\lambda$ sized, $d = 10.9\lambda$ – D1 (red crosses), D2 (blue circles). (a) PC along the u-cut for $v = 0$. (b) PC along the v-cut for $u = 0$.

with $N = 14$ and $M = 9$ PSWFs, and $d = 10.9\lambda$ (see Fig. 1). The dimensions correspond to those of the Schwarzbeck 9210d working in the 1–18 GHz band which has been subject to the next experimental analysis.

As before, two PCs, along the u-cut for $v = 0$, and along the v-cut for $u = 0$, have been considered, with D1 involving samples only along the x-axis and the y-axis, respectively. More in detail, 25 NF samples are required along the x-axis for the first PC, and 13 NF samples along the y-axis for the second PC. The D1 distributions of the two cases are reported in Fig. 6(a) and (b), respectively, as red circles. In both cases, the minimum distance between consecutive samples is about 1λ, at least doubling the classical $\lambda/2$ sampling step.

The excitation is that in (19) with $T_x = 2$ dB, $T_y = 3$ dB, $S_x = 0.4$, and $S_y = 2$. In particular, the values for the defocusing factors are larger than those in Case AP1 to investigate larger values for ϱ. Indeed, $\varrho = -5.6$ dB and $\varrho = -2.8$ dB are obtained for the u-cut and the v-cut case, respectively. With these values, even a unitary $cond(\underline{\underline{S}})$ would lead to $\varepsilon_{max} \cong 50\%$; therefore, in this case the distribution D2 is needed.

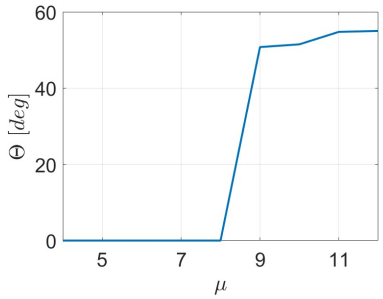

Fig. 7. Behavior of Θ as function of μ— aperture $6.4\lambda \times 3.6\lambda$ sized, d = 10.9λ, PC along the u-cut for $v = 0$.

As discussed in Section III, D2 has been obtained after iteratively adding sampling points increasing Θ, the angle between B_1 and B_2. For D2 a nonuniform raster scan grid has been considered, made of nonuniformly spaced rows, with samples therein nonuniformly spaced. The resulting grid is made of μ rows and ν columns, where $\nu = Int[N\mu/M]$.

For the sake of brevity, the behavior of Θ as function of μ is shown for the PC u-cut only (see Fig. 7). As it can be observed, Θ jumps abruptly as soon as μ reaches M, with $cond(\underline{\underline{U}}) \cong 2$, [see (18)]. Accordingly, reasonably small errors on $\underline{b}$ provide reasonably small error on $\underline{b}_1$ (just slightly increased). In particular, if the data are corrupted by a noise with a signal-to-noise ratio of 40 dB, the error on $\underline{b}_1$ would be equal to -34 dB.

A similar analysis has been performed for the PC v-cut.

Fig. 6(a) and (b) shows D2 for the two PCs as blue circles. In both cases, D2 is made of 126 points, with a minimum distance greater than 1λ, again at least doubling the classical $\lambda/2$ sampling step.

The directivity retrieved by using D1 + D2 (red line) is reported for the PCs u-cut and v-cut in Fig. 8(a) and (b), respectively, together with the numerical reference (blue crosses) and the directivity obtained by using D1 only (green dash-dotted line). As it clearly appears, in this case D2 is essential to guarantee a good characterization, as confirmed by the error figures in Table I: rows four and six of refer to the reconstruction obtained by using D1 + D2 along the u-cut and the v-cut, respectively, while rows five and seven to the case wherein only D1 is exploited. For the v-cut, only ϵ_{amp} and ϵ_{Dmax} have been reported since they are the only meaningful error figures.

Finally, let us compare the number of NF samples required by PCs and WC. PC for the u-cut requires 151 samples: 25 D1 samples and the further 126 D2 samples, arranged on nine rows. For WC, the SVO [2] provides 476 samples arranged on 17 rows. The measurement time is halved if we assume, as mentioned, that a rough estimate for the time saving is obtained by comparing the number of rows. If a standard half-wavelength sampling over a $40\lambda \times 40\lambda$ grid, is adopted for WC, the PC measurement time would be, at least, equal to 1/9 of that of WC. However, as cited in the conclusions, in this case, the expected time saving is larger since a smart controller can profit of the nonuniform samples spacings [18], [19].

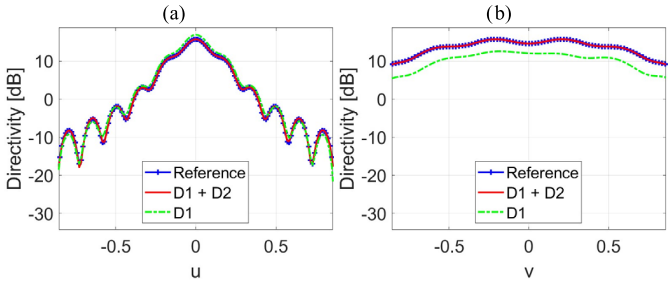

Fig. 8. Behavior of the reference directivity (blue crosses), of the one reconstructed by using the D1 and the D2 (red line), and of the one reconstructed by using only the D1 (green dash-dotted line) for an aperture $6.4\lambda \times 3.6\lambda$ sized, $d = 10.9\lambda$. (a) Reconstruction along the u-cut for $v = 0$. (b) Case reconstruction along the v-cut for $u = 0$.

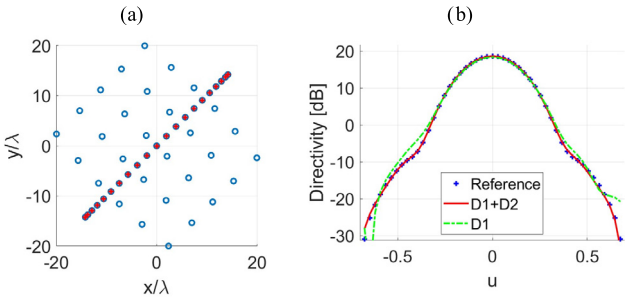

Fig. 9. (a) Sampling point distribution for an aperture $3\lambda \times 2.4\lambda$ sized, $d = 10.8\lambda$—D1 (red crosses), D2 (blue circles), PC along the cut for $u = v$. (b) Behavior of the reference directivity (blue crosses), of the one reconstructed by using the D1 and the D2 (red line), and of the one reconstructed by using only the D1 (green dash-dotted line).

C. Case AP3

The same aperture as case AP1 has been considered here, while for the excitation the data adopted for case AP1.1 are exploited.

The PC is performed along the cut for $u = v$. The approach gives a D1 involving samples along the direction $x = y$: 21 NF samples are obtained, with a minimum distance between consecutive samples greater than 0.5λ. D2 seems necessary since $\varepsilon_{max} = 75\%$. In Fig. 9(a) D1 and D2 are presented, by highlighting the D2 samples as blue circles, and the D1 ones as red crosses. D2 is made of 30 points, with a minimum distance greater than 3λ.

In this case, even if the same aperture and excitation of case AP1.1 are considered, a higher number of NF lines is needed now. This is an obvious consequence of matching with the selected FF cut orientations, the specific characteristics of the radiating AF in one case instead of the other.

The directivity reconstructed by using D1 + D2 (red line) is reported in Fig. 9(b) with the numerical reference (blue crosses) and the directivity obtained by using D1 only (green dash-dotted line).

The error figures in Table I confirm the usefulness of D2: rows eight and nine of Table I refer to the reconstruction obtained by using D1 + D2 and D1, respectively.

D. Case AP4

This case refers to a slotted waveguide array, simulated with Altair FEKO, made of eight elements, working at 10 GHz,

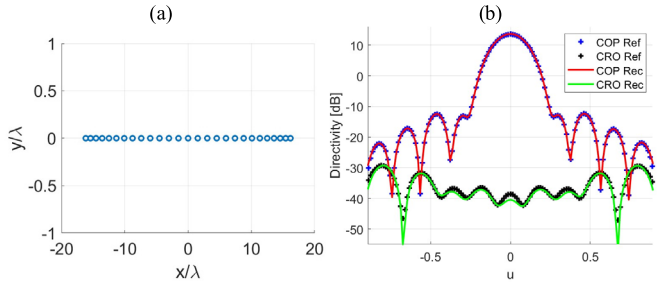

Fig. 10. (a) Sampling point distribution for an aperture 2.8 × 0.4λ sized, $d = 10\lambda$, PC along the cut for $v = 0$. (b) Behavior of the reference directivity for the co-polar (blue crosses) and the cross-polar (black crosses), and of the one reconstructed for the copular (red line) and the cross-polar (green line).

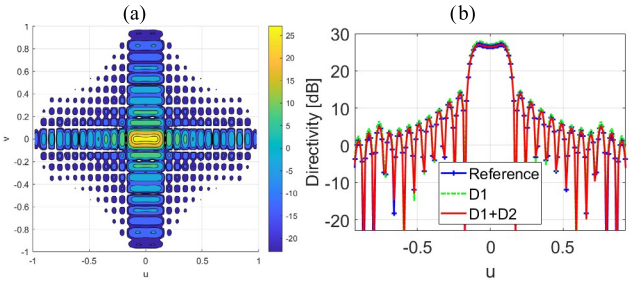

Fig. 11. (a) Synthesized directivity for the 25 × 17 array, 0.6λ spacings. (b) Behavior of the reference directivity (blue crosses), of the one reconstructed by using the D1 and the D2 (red line), and of the one reconstructed by using only the D1 (green dash-dotted line) for the synthesized array, $d = 10\lambda$. Reconstruction along the u-cut for $v = 0$.

with the slots (0.5λ × 0.05λ wide) directed along the x-axis, with a center-to-center spacing of 0.7λ and 0.1λ along x and y, respectively. The aperture parameters are $a_{ap} = 2.8\lambda$ and $b_{ap} = 0.4\lambda$, $N = 13$ and $M = 3$ PSWFs, $d = 10\lambda$ (see Fig. 1). The retrieved FFP has been compared to the one obtained after a standard WC, exploiting the NF data simulated over a 40λ × 40λ grid, with half-wavelength sampling.

The PC along u-cut for $v = 0$ has been considered, and both the co-polar and the cross-polar components have been calculated, using the Ludwig's third definition. The approach gives a D1 involving samples along the x-axis, exploited to collect both the x and the y NF components, with 27 NF samples. The D1 distribution is reported in Fig. 10(a), as blue circles: the minimum distance between consecutive samples is about 0.7λ. The obtained values for the relative error bound are $\varepsilon_{max} = 10\%$ and $\varepsilon_{max} = 15\%$ for the y and x components, respectively. The performance of the approach is evaluated with noise free data, since we are interested here in verifying the PC performance only, due to the low values of the cross-polar components. Obviously, when noisy data are considered, the error increases, as shown in the other cases, but without undesired effects due to instability.

The retrieved co-polar (red line) and cross-polar (green line) directivity are reported in Fig. 10(b), together with the numerical reference, co-polar (blue crosses) and cross-polar (black crosses). The agreement for both co-polar and cross-polar is good. The error figures are reported in rows 10 and 11 of Table I, for the co-polar and the cross-polar, respectively.

E. Case AR1

A planar array of 25 × 17 elements with an interelement spacing of 0.6λ in both directions has been considered.

The array excitations have been obtained by discretizing the continuous AF provided by a power pattern synthesis technique, wherein the complex AF is optimized following the generalized projections approach [20]. The antenna has been synthesized to radiate a shaped beam pattern with a flat-top behavior along the u-cut, and a pencil beam behavior along the v-cut. The synthesized directivity pattern is reported in Fig. 11(a).

The PC approach along the u-cut for $v = 0$ has been considered with $d = 10\lambda$. The approach identifies a D1 involving samples along the x-axis: 51 NF samples are obtained, with

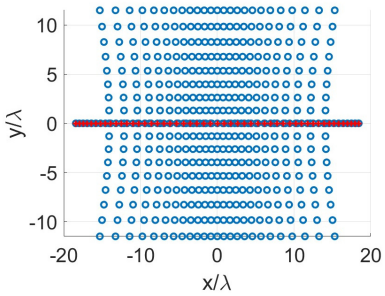

Fig. 12. Sampling point distribution for an array of 25 × 17 elements, 0.6λ spacings, $d = 10\lambda$—D1 (red crosses), D2 (blue circles), PC along the u-cut for $v = 0$.

a minimum distance between consecutive samples equal to about 0.45λ. D1 is shown in Fig. 10 as red crosses. D2 seems necessary since $\varrho = -19$ dB and $\varepsilon_{max} = 22\%$.

In Fig. 12 D1 and D2 are presented by highlighting the D2 samples as blue circles. D2 is made of 425 points, arranged on 17 rows, with a minimum distance greater than 0.7λ.

The directivity reconstructed by using D1 + D2 (red line) is reported in Fig. 11(b), together with the numerical reference (blue crosses) and the directivity obtained by using D1 only (green dash-dotted line). Again, D2 has proved essential for good performance, as confirmed by the error figures in Table I, rows 12 and 13 refer to the case wherein D1 + D2 and D1 only, respectively, are exploited.

As before let us compare the number of NF samples required by PCs and WC. PC for the u-cut requires 476 samples: 51 D1 samples and the further 425 D2 samples, arranged in 17 rows. For WC, the SVO [2] provides 1617 samples arranged in 33 rows. The measurement time is halved if we assume, as mentioned, that a rough estimate for the time saving is obtained by comparing the number of rows. Finally, if a standard half-wavelength sampling over a 40λ × 40λ grid is adopted for WC, the PC measurement time would be, at least, equal to 17/81 of that of WC.

F. Case AR2

A planar array of 25 × 25 elements with an interelement spacing of 0.6λ in both directions has been considered, synthesized to a radiated beam that steered along the direction ($u_b = 0.3$, $v_b = 0.2$). The expansion coefficients, in amplitude, have been obtained by discretizing the continuous AF in (19)

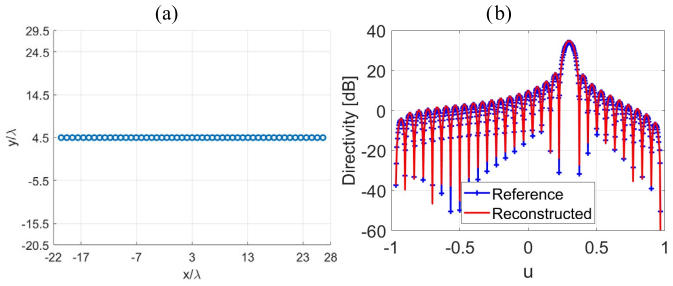

Fig. 13. (a) Sampling point distribution D1. PC along the u-cut for $v = 0.2$. (b) Behavior of the reference directivity (blue crosses) and of the one reconstructed with the D1 (red line). Reconstruction along the u-cut for $v = 0.2$ – array of 25 × 25 elements, 0.6λ spacings, $d = 10\lambda$.

with $T_x = 4$ dB, $T_y = 3$ dB, $S_x = 0$, and $S_y = 0$, and by adding linear phase terms to get the desired beam-pointing angle.

The PC has been performed along the u-cut for $v = 0.2$, with $d = 10\lambda$. The approach identifies a D1 involving samples on the line $y = 4.5\lambda$: 51 NF samples are obtained, with a minimum distance between consecutive samples of about 0.9λ. D1 is shown in Fig. 13(a) and $\varrho = -22$ dB is obtained.

In Fig. 13(b), the reconstructed directivity (red line) is shown together with the numerical reference (blue crosses), and a good agreement is observed. The error figures are reported in row 14 of Table I.

V. Experimental Results

Two antennas have been characterized in the Anecoich Chamber of Laboratorio di Microonde ed Onde Millimetriche at Università di Napoli Federico II: the standard gain horn Narda 640 and the Schwarzbeck 9210d. These antennas have been already considered in the numerical analysis. For both, a standard half-wavelength NF acquisition has been performed to evaluate the reference FFP along the cuts of interest.

Narda 640 has been characterized at 9.4 GHz. A picture of the measurement setup is shown in Fig. 14(a). As for the case AP1, two PCs, along the u-cut for $v = 0$, and along the v-cut for $u = 0$, have been considered. The measurements have been performed by using the two distributions D1 in Fig. 4 (Case AP1). The FFP cut reconstructed with D1 (red line) is reported for the u-cut along $v = 0$ and the v-cut for $u = 0$ in Fig. 14(b) and (c), respectively, together with the reference (blue crosses). As it can be observed a good agreement is obtained.

The meaningful error figures are

1) $\epsilon_{amp} = 3.2\%$, $\epsilon_{3dB} = 0\%$, $\epsilon_{bp} = 0\%$.
2) $\epsilon_{amp} = 3.1\%$, $\epsilon_{3dB} = 0\%$, $\epsilon_{SLL} = 2\%$, $\epsilon_{bp} = 0\%$.

for the u-cut and the v-cut, respectively, showing the good performance of the reconstruction. Regarding the normalized pattern, we have $\bar{\epsilon}_{amp} = 0.34\%$ and $\bar{\epsilon}_{amp} = 0.72\%$, for the u-cut and the v-cut, respectively.

Schwarzbeck 9210d has been characterized at 7.8 GHz. A picture of the measurement setup is shown in Fig. 15(a). For the sake of brevity, PC has been considered only along the u-cut for $v = 0$. The measurements have been collected by using the sampling points shown in Fig. 6(a) (Case AP2), wherein both D1 and the D2 are shown. The FFP reconstructed

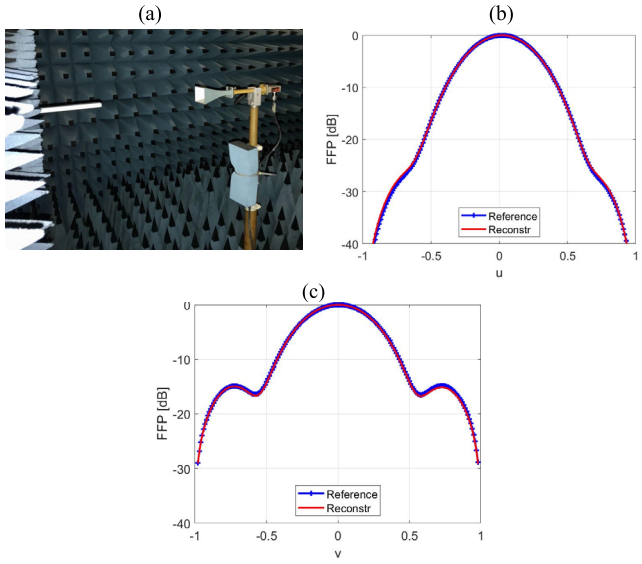

Fig. 14. (a) Photograph of the measurement setup for the Standard Gain Horn Narda 640. (b) Behavior along the u-cut for $v = 0$ of the reference FFP (blue crosses) and of the one reconstructed with the D1 (red line). (c) Behavior along the v-cut for u = 0 of the reference FFP (blue crosses) and of the one reconstructed with the D1 (red line)—Narda 640, 9.4 GHz, $d = 10.8\lambda$, experimental characterization.

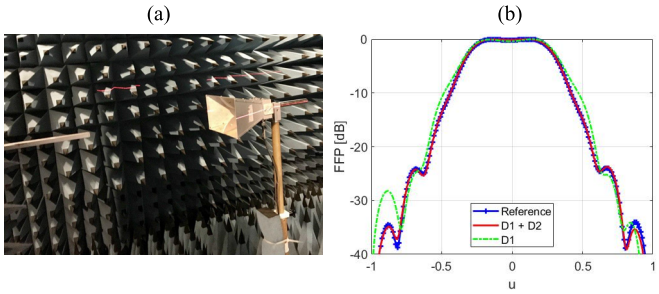

Fig. 15. (a) Photograph of the measurement setup for the Schwarzbeck 9210d. (b) Behavior along the u-cut for $v = 0$ of the reference FFP (blue crosses), of the one reconstructed by using the D1 and the D2 (red line), and of the one reconstructed by using only the D1 (green dash-dotted line)—Schwarzbeck 9210d, 7.8 GHz, $d = 10.9\lambda$, experimental characterization.

by using D1 + D2 (red line) is reported in Fig. 15(b), together with the reference (blue crosses) and the directivity obtained by using D1 only (green dash-dotted line). Again, D2 has proved essential for good performance, as confirmed by the meaningful error figures: $\epsilon_{amp} = 2\%$. By using the D1 only, we have $\epsilon_{amp} = 7.5\%$.

Regarding the normalized pattern, we have $\bar{\epsilon}_{amp} = 7.5\%$ for the two measurement configurations (D1 + D2, or only D1).

VI. Conclusion

In the framework of the NF antenna measurements, in many cases, the reconstruction of the whole FFP is not strictly required, but just the partial knowledge of the FFP along some cuts is needed. A method for PC has been proposed. The approach provides a general framework for PC and defines the optimal distribution of the NF samples required to reconstruct the FFP along the cut of interest.

The obtained sample distribution allows to reduce the measurement time with respect to WC. Indeed, as long as the

data are located along rows or columns, as well as on rings, the reduction of the number of rows/columns/rings involves an obvious reduction of the measurement time. In this case, the time reduction factor can be easily evaluated, and the time reduction is achieved for both single probe and multiprobe acquisitions.

Obviously, the probe movements impacts on the acquisition time along a single line. The reduction of the number of samples determines an obvious time reduction for acquisitions based on stepped movements (stop-and-go). On the other hand, even in the case of continuous probe movements, the reduction of samples leads to a time reduction as long as a smart control of the scanning system is adopted, profiting of the spatial nonuniformity of the samples, as shown in [18] and [19].

Finally, at difference with other methods, the approach presented here provides, in a rigorous mathematical framework, a general strategy to determine the distribution of the measurement points needed to perform a NF antenna PC according to a prefixed threshold error. The technique is able to determine if one or more NF cuts are needed, to guarantee a given reconstruction error, and to determine the optimal samples distribution minimizing the scanning path length.

REFERENCES

[1] R. Cornelius, T. Salmerón-Ruiz, F. Saccardi, L. Foged, D. Heberling, and M. Sierra-Castañer, "A comparison of different methods for fast single-cut near-to-far-field transformation [euraap corner]," *IEEE Antennas Propag. Mag.*, vol. 56, no. 2, pp. 252–261, Apr. 2014.

[2] A. Capozzoli, C. Curcio, G. D'Elia, and A. Liseno, "Singular-value optimization in plane-polar near-field antenna characterization," *IEEE Antennas Propogation Mag.*, vol. 52, no. 2, pp. 103–112, Apr. 2010.

[3] A. Capozzoli, C. Curcio, and A. Liseno, "Truncation in 'quasi-raster' near-field acquisitions [measurements corner]," *IEEE Antennas Propag. Mag.*, vol. 54, no. 5, pp. 174–183, Oct. 2012.

[4] F. D'Agostino, F. Ferrara, C. Gennarelli, R. Guerriero, and M. Migliozzi, "Reconstruction of the antenna far-field pattern through a fast plane-polar scanning," *Appl. Comput. Electromagn. Soc. J.*, vol. 31, no. 12, pp. 1362–1369, 2016.

[5] M. Sierra-Castañer and S. Burgos, "Fresnel zone to far field algorithm for rapid array antenna measurements," in *Proc. 5th Eur. Conf. Antennas Propag. (EUCAP)*, Rome, Apr. 2011, pp. 3251–3255.

[6] T. Salmerón-Ruiz, M. Sierra-Castañer, F. Saccardi, S. Burgos, F. J. Cano-Fácila, and L. J. Foged, "A fast single cut spherical near-field-to-far-field transformation using cylindrical modes," in *Proc. 8th Eur. Conf. Antennas Propag. (EuCAP)*, The Hague, The Netherlands, Apr. 2014, pp. 2476–2480.

[7] F. R. Varela, B. G. Iragüen, and M. S. Castaner, "Single-cut phaseless near-field measurements using specialized probes," in *Proc. Antenna Meas. Techn. Assoc. Symp. (AMTA)*, Denver, CO, USA, Oct. 2022, pp. 1–5, doi: 10.23919/AMTA55213.2022.9954985.

[8] A. Capozzoli, C. Curcio, and A. Liseno, "Optimized partial near field antenna characterization," presented at the 41st PhotonIcs Electromagn. Res. Symp. (PIERS), Rome, Italy, Jun. 2019.

[9] A. Capozzoli, C. Curcio, and A. Liseno, "Fast single-cut antenna characterization by near field measurements," in *Proc. 14th Eur. Conf. Antennas Propag. (EuCAP)*, Copenhagen, Denmark, Mar. 2020, pp. 1–4, doi: 10.23919/EuCAP48036.2020.9135445.

[10] A. Capozzoli, C. Curcio, G. D'Elia, and A. Liseno, "Phaseless antenna characterization by prolate function expansion of the aperture field," *Microw. Opt. Technol. Lett.*, vol. 48, no. 10, pp. 2060–2064, Oct. 2006, doi: 10.1002/mop.21852.

[11] H. Xiao, V. Rokhlin, and N. Yarvin, "Prolate spheroidal wavefunctions, quadrature and interpolation," *Inverse Problems*, vol. 17, no. 4, pp. 805–838, 2001.

[12] C. J. Bouwkamp, "On spheroidal wave functions of order zero," *J. Math. Phys.*, vol. 26, pp. 79–92, Apr. 1947.

[13] A. Osipov and V. Rokhlin, "On the evaluation of prolate spheroidal wave functions and associated quadrature rules," *Appl. Comput. Harmon. Anal.*, vol. 36, no. 1, pp. 108–142, 2014.

[14] A. Capozzoli, C. Curcio, and A. Liseno, "Different metrics for singular value optimization in near-field antenna characterization," *Sensors*, vol. 21, no. 6, p. 2122, Mar. 2021, doi: 10.3390/s21062122.

[15] R. E. Collin and F. J. Zucker, *Antenna Theory*. New York, NY, USA: McGraw-Hill, 1969.

[16] G. H. Golub and C. F. Van Loan, *Matrix Computations*, 4th ed. Baltimore, MD, USA: Johns Hopkins Univ., 2013.

[17] G. E. Shilov, *Linear Algebra*. New York, NY, USA: Dover, 1977.

[18] A. Capozzoli, L. Celentano, C. Curcio, A. Liseno, and S. Savarese, "Optimized trajectory tracking of a class of uncertain systems applied to optimized raster scanning in near-field measurements," *IEEE Access*, vol. 6, pp. 8666–8681, 2018, doi: 10.1109/ACCESS.2018.2802638.

[19] A. Capozzoli, L. Celentano, C. Curcio, A. Liseno, and S. Savarese, "Twice optimised near-field scanning system for antenna characterisation," *IET Microw., Antennas Propag.*, vol. 14, pp. 163–173, 2020, doi: 10.1049/iet-map.2019.0178.

[20] A. Capozzoli, C. Curcio, A. Liseno, and G. Toso, "Fast, phase-only synthesis of aperiodic reflectarrays using NUFFTs and CUDA," *Prog. Electromagn. Res.*, vol. 156, pp. 83–103, 2016.

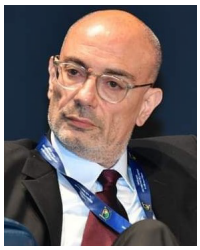

Amedeo Capozzoli (Member, IEEE) received the Laurea degree (summa cum laude) in electronic engineering and the Ph.D. degree in electronic engineering and computer science from Università di Napoli Federico II, Naples, Italy.

He is currently a Full Professor of Electromagnetic Fields with Università di Napoli Federico II. His research interests include methods to extract synthetic information on systems of sources or scatterers from field data, adaptive optics in optical astronomy, antenna synthesis and diagnosis, fast numerical methods in electromagnetics, GPU computing in electromagnetics, advanced measurement approaches in electromagnetics, inverse problems, and remote sensing.

Dr. Capozzoli is a fellow of the *Antenna Measurement Technique Association*. His honors and distinctions has been awarded include the Telecom Italia Prize for the best thesis in Electronic Engineering that was defended at Università di Napoli Federico II, the Barzilai Prize for young scientists in 2002, from the Italian Society of Electromagnetism, the Best Technical Paper Award, from the Antenna Measurement Technique Association (AMTA) in two consecutive years in 2009 and 2010, the Honorable Mention at the *5th European Conference on Antennas and Propagation* (EuCAP 2011), the Nomination for the Best Paper Award at the *8th European Conference on Antennas and Propagation* (EuCAP 2014) and at the *12th European Conference on Antennas and Propagation*(EuCAP2018). Since 2013, he has been responsible for the *Course on Antenna Synthesis* in the framework of European School of Antennas (ESoA). In December 2016, he received the 2016 Best Italian EMC Poster Prize at the IEEE EMC Young Professional Paolo Corona Day. He has been co-author of papers which received the Mini-Circuits Harvey Kaylie Best Student Paper Award at IEEE-COMCAS in 2021 and the Best Student Paper Award from the Antenna Measurement Techniques Association in 2021. He is a Founder and Chair of the Italian AMTA node, the first European node of the *Antenna Measurement Technique Association*. He is also a Chair of the Microwave and Millimeter Wave Laboratory and of the Numerical Electromagnetics Laboratory at Università di Napoli Federico II.

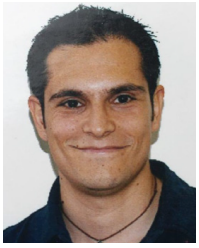

Claudio Curcio (Member, IEEE) received the Laurea degree (summa cum laude) in electronic engineering and the Ph.D. degree in electronic and telecommunication engineering from the Università di Napoli Federico II, Naples, Italy, in 2002 and 2005, respectively.

From 2006 to 2007, he held a Post-Doctoral position at Università di Napoli Federico II. He is currently an Associate Professor with Università di Napoli Federico II. His research interests include antenna measurements, standard and phaseless effective near-field/far-field transformation techniques, optical beamforming techniques for array antennas, array, and reflectarray synthesis.

Dr. Curcio has been a member of the IEEE Working Group for the revision of the Standard IEEESTD1720 "Recommended Practice for Near-Field Antenna Measurements," since May 2020. In February 2002, he won the Optimus Award at the SIMAGINE, "Worldwide GSM & Java Card Developer Contest." In 2009 and 2010, he received the Best Technical Paper Award at the *Antenna Measurement Techniques Association Symposium*. In 2011, he was a recipient of the Honorable Mention for the Best Antenna Measurement Paper at the *European Conference on Antennas and Propagation* (EUCAP), in 2013 and 2018, he was the finalist for the Antenna Measurements Best Paper Award at the EUCAP. In the 2016, he received the IEEE Best Italian EMC Poster Prize from the IEEE EMC Society, Italy Chapter. He is an Academic Editor of *International Journal of Antennas and Propagation* (Wiley's) and IEEE ACCESS.

Angelo Liseno was born in Italy, in 1974. He received the Laurea degree (summa cum laude) and the Ph.D. degree in electrical engineering from the Seconda Università di Napoli, Aversa, Italy, in 1998 and 2001, respectively.

From 2001 to 2002, he was a Post-Doctoral with the Seconda Università di Napoli. From 2003 to 2004, he was a Research Scientist with the Institut für Hochfrequenztechnik und Radarsysteme, Deutsches Zentrum für Luft- und Raumfahrt (DLR), Oberpfaffenhofen, Germany. From 2005 to 2015, he was a Researcher with the Dipartimento di Ingegneria Elettrica e delle Tecnologie dell'Informazione, Università di Napoli Federico II, Naples, Italy, where he has been an Associate Professor, since 2015. His research interests include parallel computing techniques for electromagnetics, general purpose GPU computing, complex and phaseless near-field/far-field transformation techniques, antenna synthesis, remote sensing, and inverse scattering, imaging and tomography.

Dr. Liseno was awarded the Best Technical Paper Award from the *Antenna Measurement Techniques Association* (AMTA) in two consecutive years in 2009 and 2010, the Honorable Mention for the Best Antenna Measurement Paper at the *European Conference on Antennas and Propagation* in 2011, the Nomination for the Best Paper Award at the *8th European Conference on Antennas and Propagation*(EuCAP 2014) and at the *12th European Conference on Antennas and Propagation* (EuCAP2018) and the Best Italian EMC Poster Prize from the IEEE EMC Society, Italy Chapter, in 2016. He is Academic Editor of *International Journal of Antennas and Propagation* and *Advanced Electromagnetics* (Wiley's) and *IET Microwaves*, *Antennas* and *Propagation*.

Open Access funding provided by 'Università degli Studi di Napoli "Federico II"' within the CRUI CARE Agreement